ADVANCED OPTICAL MATERIALS
www.advopticalmat.de

Large Mid-Infrared Magneto-Optic Response from Doped Cadmium Oxide at Its Epsilon-Near-Zero Frequency

*Jonathon R. Schrecengost, Angela J. Cleri, Maxwell J. Tolchin, Ramya Mohan, John P. Murphy, Sara Adamkovic, Alex J. Grede, Mario V. Imperatore, Patrick E. Hopkins, Jon-Paul Maria, and Noel C. Giebink**

The epsilon-near-zero (ENZ) frequency regime of transparent conducting oxide materials is known to yield large enhancements in their optical nonlinearity and electro-optic response. Here, Faraday rotation is investigated in Gd and In-doped CdO films and it is found that the Verdet constant peaks at values >3 10^5 deg T^{-1} m^{-1} near the ENZ frequency, which is tunable in the wavelength range 2 < λ < 10 µm by varying the doping concentration. These results are among the highest reported to date in the mid-infrared spectral range and are in good agreement with the Drude model, which confirms that the magneto-optic response of doped CdO derives from its free carriers. The combination of a tunable Verdet constant, low optical loss compared to other plasmonic materials, and the ability to deposit CdO on Si with no loss in performance make this material a promising platform for integrated magneto-optic and magnetoplasmonic devices that operate across the mid-infrared.

1. Introduction

Transparent conducting oxide (TCO) materials are promising for a variety of plasmonic and nanophotonic applications because their plasma frequency can be varied across the near- and mid-infrared spectrum (NIR and MIR, collectively spanning the wavelength range 1 < λ < 10 µm), they possess low optical loss compared to noble metals, and many of them are CMOS-compatible.[1,2] This combination of characteristics is particularly valuable for integrated photonics because it provides a path to shrink the footprint of devices such as electro-optic modulators and phase shifters,[3,4] and because it facilitates large optical nonlinearity in the vicinity of the epsilon-near-zero (ENZ) frequency.[5,6] The nonlinearity enhancement is mainly a slow light effect and can be understood from the differential relationship between refractive index and relative dielectric constant, $\Delta n = \Delta\epsilon/2n$, which shows that a given change in dielectric constant ($\Delta\epsilon$) yields a large change in refractive index (Δn) when n becomes small near the ENZ frequency.[7]

Given the generality of this scaling relationship, ENZ enhancement applies, not just to optical nonlinearity, but to any type of dielectric constant perturbation such as, for example, that resulting from an applied electric or magnetic field. While the former is driving intense interest for electro-optic modulators,[3,4,8] the latter remains largely unexplored in TCO materials[9,10] despite the fact that

J. R. Schrecengost, A. J. Cleri, M. J. Tolchin, J.-P. Maria
Department of Materials Science and Engineering
The Pennsylvania State University
University Park, PA 16802, USA

R. Mohan, P. E. Hopkins
Department of Mechanical and Aerospace Engineering
University of Virginia
Charlottesville, VA 22904, USA

R. Mohan, P. E. Hopkins
Department of Materials Science and Engineering
University of Virginia
Charlottesville, VA 22904, USA

The ORCID identification number(s) for the author(s) of this article can be found under https://doi.org/10.1002/adom.202400803

DOI: 10.1002/adom.202400803

J. P. Murphy, S. Adamkovic, A. J. Grede, M. V. Imperatore, N. C. Giebink
Department of Electrical Engineering
The Pennsylvania State University
University Park, PA 16802, USA
E-mail: ngiebink@umich.edu

J. P. Murphy, A. J. Grede
NRC postdoc residing at the US Naval Research Laboratory
Washington, DC 20375, USA

P. E. Hopkins
Department of Physics
University of Virginia
Charlottesville, VA 22904, USA

N. C. Giebink
Department of Electrical Engineering and Computer Science
University of Michigan
Ann Arbor, MI 48109, USA

plasma-enhanced magneto-optic (MO) effects are well-known for ferromagnetic metals[11–14] and degenerately doped semiconductors such as InSb[15] and InAs.[16] In this context, TCOs could fill a gap in MO response between garnet-based materials in the NIR[17,18] and InSb in the long-wave infrared,[15] providing a CMOS-compatible platform for the integration of MO isolators,[19] circulators,[20,21] linear ↔ circular[22,23] polarizers, and sensors[24] in MIR Si photonics.[25,26]

Here, we carry out Faraday rotation spectroscopy on In- and Gd-doped CdO films in which the ENZ frequency is tuned throughout the NIR-MIR by varying the dopant concentration. We find that the Verdet constant increases with wavelength and peaks near the ENZ frequency, yielding values $>3\bullet10^5$ deg T^{-1} m^{-1} that are accurately predicted by classical Drude theory. Importantly, doped CdO can be grown on Si with no loss in performance, and its Faraday rotation does not saturate at high magnetic field strength (measured up to 3 Tesla), making it a promising platform for non-reciprocal photonic circuit elements in the MIR. Additionally, the theory predicts a peak in magnetic circular dichroism near the ENZ frequency, which may prove useful for magnetic field-tunable circular polarizers[23] or other MO devices.

2. Theory

The dielectric function of doped CdO is well-described by the Drude model in the NIR-MIR frequency range.[27] In the presence of a $\hat{z}$-directed magnetic field B, the normally isotropic response of the free carrier plasma becomes uniaxial and gyrotropic, with a frequency-dependent complex permittivity tensor given by:[16,28]

$$\boldsymbol{\varepsilon}(\omega) = \varepsilon_0 \begin{pmatrix} \varepsilon_{xx} & -ig & 0 \\ ig & \varepsilon_{xx} & 0 \\ 0 & 0 & \varepsilon_{zz} \end{pmatrix} \tag{1a}$$

$$\varepsilon_{xx} = \varepsilon_{yy} = \varepsilon_\infty - \frac{\omega_p^2(\omega + i\gamma)}{\omega\left[(\omega + i\gamma)^2 - \omega_c^2\right]} \tag{1b}$$

$$g = \frac{-\omega_p^2 \omega_c}{\omega\left[(\omega + i\gamma)^2 - \omega_c^2\right]} \tag{1c}$$

$$\varepsilon_{zz} = \varepsilon_\infty - \frac{\omega_p^2}{\omega(\omega + i\gamma)} \tag{1d}$$

where $\omega_c = eB/m^*$ is the cyclotron frequency. Details of the derivation are provided in the Supplementary Material. As usual, the plasma frequency $\omega_p = \sqrt{Ne^2/(m^*\varepsilon_0)}$, is set by the free carrier density (N) and effective mass (m^*), while the damping frequency $\gamma = \frac{e}{\mu_{opt} m^*}$, is parameterized in terms of the optical mobility (μ_{opt}). In all of these expressions, e is the elementary charge, ϵ_0 is the permittivity of free space, and the angular frequency of light (ω) is related to the free space wavelength (λ) via the speed of light in vacuum (c) according to $\omega = 2\pi c/\lambda$. The value of ω that results in $\mathrm{Re}[\varepsilon_{xx}] = 0$ is known as the ENZ frequency. It is related to ω_p via the high-frequency dielectric constant (ε_∞) by solving Equation (1b) to yield $\omega_{ENZ} \approx \omega_p/\sqrt{\varepsilon_\infty}$. All of the Drude material parameters (N, m^*, μ_{opt}, and ε_∞) have been extensively characterized for CdO[27–29] and indium-tin-oxide (ITO)[15,30] through a combination of variable angle spectroscopic ellipsometry and Hall measurements. The optical phonon contribution to the dielectric function is negligible at MIR wavelengths owing to its low frequency (266 cm^{-1}).[27]

Following refs. [31,32], light with electric field amplitude, E_0, propagating in the $\hat{z}$ direction will undergo Faraday rotation in the Drude plasma under an applied magnetic field, $B\hat{z}$, due to the off-diagonal elements in Equation (1a). Assuming the light is linearly polarized in the $\hat{x}$-direction starting at $z = 0$, Maxwell's equations provide the solution for $E(z,t)$, which is a linear combination of the eigenmodes that represent right(+) and left(-) circularly polarized light:

$$\boldsymbol{E}(z,t) = E_0\left[\cos\left(\frac{\omega\Delta n z}{c}\right)\hat{x} - \sin\left(\frac{\omega\Delta n z}{c}\right)\hat{y}\right] e^{-i\omega\left(t - \frac{n_0 z}{c}\right)} \tag{2}$$

where $n_\pm = \sqrt{\varepsilon_{xx} \pm g}$ are the corresponding complex refractive indices associated with each polarization and their average, $n_0 \equiv (n_+ + n_-)/2$, and difference $\Delta n \equiv (n_+ - n_-)/2$, are defined for convenience. The difference in refractive index for right and left-circularly polarized light can be intuitively understood from the opposite sign of the Lorentz force for right and left-circulating electrons driven by the rotating electric field, which effectively changes the radius of their orbit and thus the polarizability in each case. Starting from a linear polarization state, the phase difference that accumulates between the left and right circular polarization components as they propagate axially at different speeds through the material along B causes the linear polarization vector to rotate by an angle, θ, from its initial orientation. This is known as magnetic circular birefringence, or Faraday rotation. The rotation angle can be determined from the x and y components of $\boldsymbol{E}$ via,

$$\tan 2\theta = \frac{2\,\mathrm{Re}\{\chi\}}{1 - |\chi|^2} \tag{3}$$

where the ratio $\chi \equiv \frac{E_y}{E_x} = \frac{-\sin(\omega\Delta n z/c)}{\cos(\omega\Delta n z/c)}$ is generally complex since Δn is complex.

The imaginary component of Δn, which arises from a magnetically induced difference in the absorption of right- and left-circularly polarized light, causes linearly polarized light to become elliptical and is known as magnetic circular dichroism (MCD), or Faraday ellipticity. Faraday ellipticity is characterized by an angle, $\psi = \tan^{-1}[B/A]$, where A is the major and B is the minor axis of the ellipse traced by the polarization vector. The ellipticity angle thus exists in the range $-45° \le \psi \le 45°$ and can be calculated by:[32]

$$\sin 2\psi = \frac{2\,\mathrm{Im}\{\chi\}}{1 + |\chi|^2} \tag{4}$$

Table 1. Summary of the TCO samples studied in this work; additional samples are provided in the Supporting Information. The Drude parameters N, μ_{opt}, m^*, and ε_∞ are fit from spectroscopic ellipsometry. Samples S1-S7 are deposited on 430 µm-thick c-plane sapphire (Al_2O_3) substrates, whereas the ITO is a commercially grown sample on 1 mm-thick soda lime glass. The numbering of the samples reflects the order in which they were grown. Samples S7 and S8 have similar doping concentrations to S2; however, the dopant in S7 is indium whereas the substrate for S8 is 280 µm-thick (100) Si.

name	dopant	ENZ [nm]	N [cm^{-3}]	μ_{opt} [$cm^2\ V^{-1}\ s^{-1}$]	m^* [m_e]	ε_∞	thickness [nm]	substrate
S1	In	1857	$4.65\cdot10^{20}$	200	0.27	5.3	2100	Al_2O_3
S2	Gd	2186	$2.8\cdot10^{20}$	200	0.225	5.3	970	Al_2O_3
S3	Gd	3491	$9.0\cdot10^{19}$	200	0.18	5.4	650	Al_2O_3
S4	Gd	4096	$6.5\cdot10^{19}$	200	0.175	5.5	590	Al_2O_3
S5	Gd	6065	$2.6\cdot10^{19}$	200	0.15	5.5	2350	Al_2O_3
S6	None	11118	$8\cdot10^{18}$	200	0.14	5.55	2560	Al_2O_3
ITO	–	1186	$1.02\cdot10^{21}$	15	0.34	3.6	400	soda-lime glass
S7	In	2264	$2.55\cdot10^{20}$	230	0.22	5.3	620	Al_2O_3
S8	Gd	2186	$2.85\cdot10^{20}$	175	0.225	5.3	1970	Si

The Verdet constant, Θ, and specific Faraday ellipticity, Ψ, which are material properties defined per unit magnetic field per unit propagation length, are then given by:

$$\Theta \equiv \frac{\theta}{zB} = \frac{1}{2zB}\tan^{-1}\left(\frac{2\,\mathrm{Re}\{\chi\}}{1-|\chi|^2}\right) \tag{5}$$

and

$$\Psi \equiv \frac{\psi}{zB} = \frac{1}{2zB}\sin^{-1}\left(\frac{2\,\mathrm{Im}\{\chi\}}{1+|\chi|^2}\right) \tag{6}$$

respectively. Finally, because light is attenuated as it propagates through the material due to linear absorption, it is useful to define a MO figure of merit, F, that quantifies Faraday rotation per unit loss according to,

$$F \equiv \frac{\Theta}{\alpha_{max}} \tag{7}$$

where $\alpha_{max} = \max[2\omega \cdot (\mathrm{Im}\{n_0\} + \mathrm{Im}\{\Delta n\})/c]$ is the larger of the two absorption coefficients associated with left and right-circularly polarized light in the medium.[31] Using the Drude expressions for $\varepsilon(\omega)$ in Equation (1), it is straightforward to numerically evaluate Θ, Ψ, and F in Equations (5)–(7), respectively. We opt not to use the transparent approximation for Θ and F described in refs. [14,31] because they fail in the ENZ regime as shown in Supplementary Material Figure S1 (Supporting Information).

3. Results

Table 1 summarizes the ellipsometry-derived Drude dielectric function parameters[27] for a series of CdO films deposited by high-power impulse magnetron sputtering (HiPIMS) with varying thickness, dopant type (Gd vs In), and doping concentration that result in ENZ wavelengths spanning the range ~2 to ~11 µm. These particular dopants are chosen because they yield CdO films with comparable electronic and optical properties, but differ in their magnetic response (i.e., Gd is paramagnetic while In is diamagnetic). Photographs of typical high optical quality 500 nm thick Gd-doped CdO films deposited on (100) Si and c-plane sapphire (c-Al_2O_3) are shown in **Figure 1a,b**, respectively. Consistent with ref. [27], the electron effective mass increases monotonically with doping concentration due to the non-parabolicity of the CdO conduction band. Compared to commercial indium-tin-oxide (ITO, Colorado Concept Coatings), CdO has a smaller effective mass and much higher electron mobility, both of which are

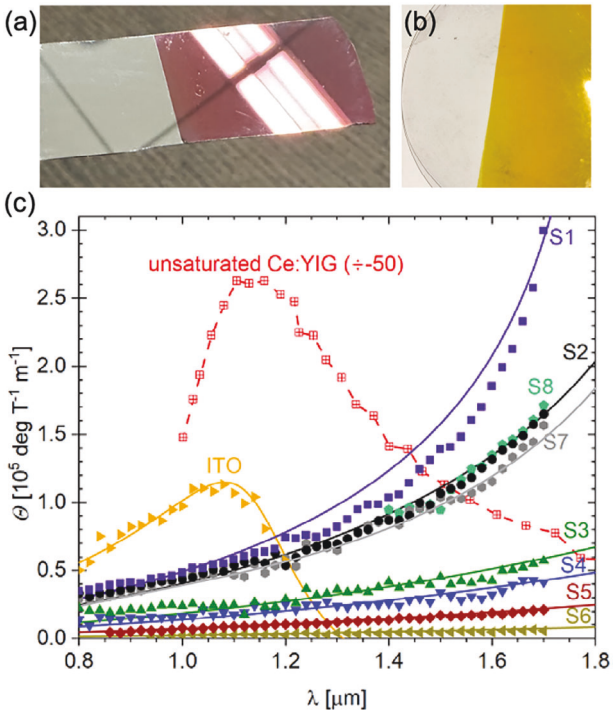

Figure 1. Photographs of optical quality doped CdO films on (a) Si and (b) sapphire substrates where the film has been etched off on the left-hand side of each substrate. c) The measured Verdet constant of doped CdO increases with wavelength (samples S1–S6), whereas other state-of-the-art materials such as Ce:YIG[17] decrease into the NIR and MIR. Solid lines are calculated from Equation (5) in the text using the parameters in Table 1. Note, the fit line for sample S8 is difficult to see because it lies underneath that of sample S2.

advantageous from an MO standpoint as discussed below. The high mobility of doped CdO originates from the fact that aliovalent cations such as Gd and In displace many of the native oxygen vacancies in the CdO lattice. Because the dopant ions have a smaller Coulomb scattering cross-section and perturb the lattice less than the native oxygen vacancies, doping decreases the rate of impurity scattering in CdO, thereby increasing its mobility.[33]

Faraday rotation spectroscopy is carried out in the NIR spectral range from 0.8–1.7 μm using the MO polarimeter detailed in the Experimental section. The Verdet constant is calculated at each wavelength by measuring the rotation angle as a function of B, subtracting the contribution from the bare substrate, and then dividing the slope of the resulting data by the film thickness obtained from mechanical profilometry or atomic force microscopy (AFM). The source data and analysis procedure are provided in Figures S2–S4 (Supporting Information). The results in Figure 1c show that doped CdO films possess large Verdet constants that increase with doping concentration and exhibit anomalous dispersion in the NIR (i.e., Θ increases with wavelength), in contrast to state-of-the-art dielectric MO materials,[32] such as Ce:YIG crystals[17] and Dy_2O_3 ceramics.[34] For films with similar carrier concentrations, the measured Verdet constants are independent of film thickness (Supplementary Material Figure S2, Supporting Information), dopant type (Gd in sample S2 vs In in sample S7), and substrate (c-Al_2O_3 for sample S2 vs (100) Si for sample S8). Within the telecom band at $\lambda = 1.55$ μm, the Verdet constant of the most highly doped CdO film (S1) is ≈80x larger than Dy_2O_3 ceramics,[34] but 30x smaller than state-of-the-art Ce:YIG (Figure 1c) when evaluated below its saturation magnetization.[17]

A key takeaway from Figure 1c is the close agreement between the measured data and the Drude model prediction for all of the TCO samples using Equation (5) with the values of N, μ_{opt}, m^* and ε_∞ obtained from ellipsometry in Table 1. The accuracy of the Drude description in Figure 1c indicates that Faraday rotation in doped CdO originates purely from the free carrier response and therefore can be reliably extrapolated into the ENZ regime at longer wavelengths as shown in **Figure 2**a. Comparing these results with the real part of the dielectric function (ε') plotted in Figure 2b demonstrates that Θ peaks slightly to the blue of λ_{ENZ} (indicated by the vertical dashed line segments) at a wavelength where the group refractive index peaks. The case of ITO is noteworthy in this context since its ENZ wavelength falls within the NIR measurement range, confirming that the Drude model remains accurate in the ENZ regime.

The theoretical model affords further insight into how each of the Drude parameters, N, ε_∞, m^*, and μ_{opt}, affect Θ; details are provided in Supplementary Material Figure S5 (Supporting Information). In addition to decreasing λ_{ENZ}, increasing N also boosts the peak Verdet constant since there are more free carriers to contribute to the MO response. Lowering ε_∞ slightly blueshifts λ_{ENZ}, but does not affect the shape or magnitude of the Verdet constant dispersion. Decreasing m^* increases the plasma frequency (thus decreasing λ_{ENZ}) and, more importantly, increases the cyclotron frequency which strengthens the MO response and leads to higher peak values of Θ. As explained in refs. [27,29], m^* in CdO increases with N due to carrier filling of its non-parabolic conduction band; this effect is what causes Θ to remain roughly as large in the MIR for low-doped samples (e.g., sample S6) as it is in the NIR for high-doped samples (e.g., sample S1). Increasing μ_{opt} increases the peak value of Θ, but only in a narrow bandwidth around λ_{ENZ}. The analysis in Supplementary Material Figure S5 (Supporting Information) makes it clear that the higher mobility and lower effective mass of doped CdO are the origin of its enhanced MO response compared to ITO.[10]

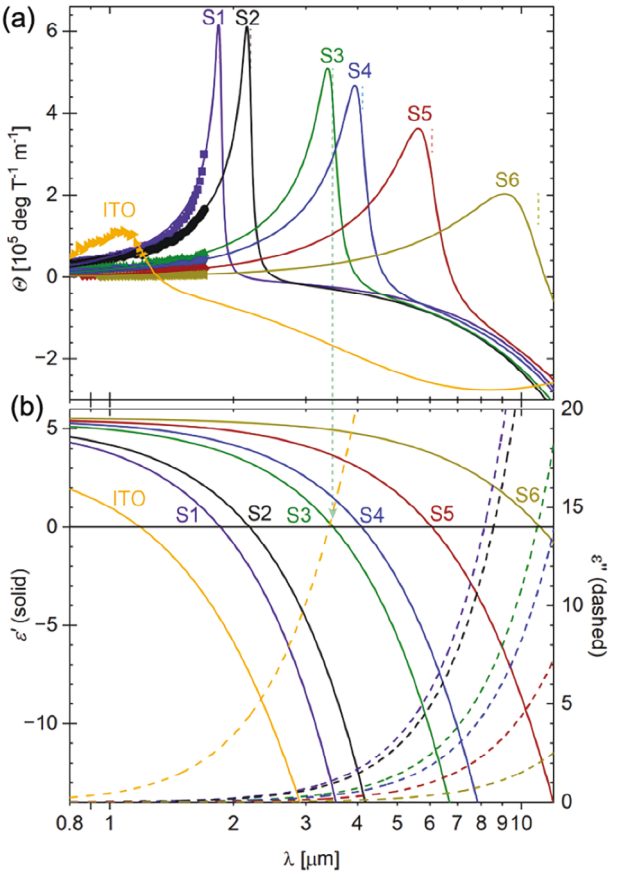

Figure 2. a) Measured Verdet constants (symbols) from Figure 1c shown together with their Drude model predictions (solid lines, Equation (5)) extrapolated to longer wavelengths. b) Real (ε', solid lines) and imaginary (ε'', dashed lines) components of the permittivity for each sample calculated from Equation (1b) using the Drude parameters in Table 1. The peak in Θ approximately coincides with the ENZ wavelength where ε' = 0 as emphasized by the vertical dashed lines in (a). The breadth of the Θ peak increases moving into the MIR because the damping frequency (γ) remains roughly constant while the ENZ frequency decreases, thus leading to a fractional increase in Θ linewidth at longer wavelengths.

Since all TCO films attenuate strongly at wavelengths beyond λ_{ENZ} due to the increase in the imaginary component of the dielectric function (ε'' in Figure 2b), it is important to assess their MO figure of merit in **Figure 3**. Below λ_{ENZ}, increasing absorption offsets the increase in Θ, causing F to remain approximately constant, irrespective of doping. Although the plateau in F is independent of doping, it is important to remember that doping strongly affects the magnitude of Θ at a given wavelength (Figure 2a), which in turn impacts the magnetic field strength and/or propagation length required to achieve a given rotation. As shown in Supplementary Material Figure S6a, F is proportional to μ_{opt} for wavelengths below λ_{ENZ}, which is why the CdO

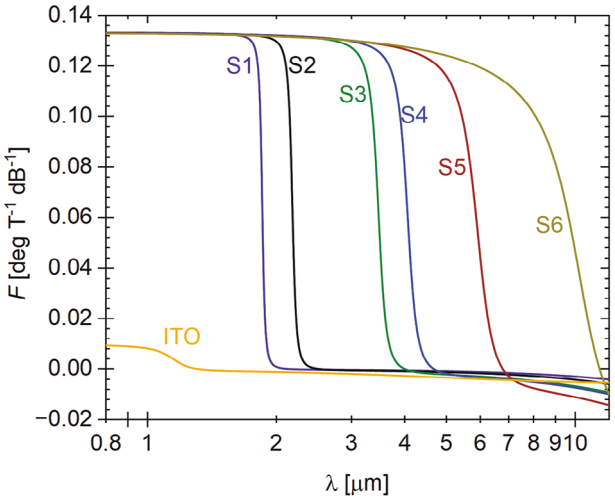

Figure 3. MO figure of merit calculated for samples S1-S6 and ITO using Equation (7).

figure of merit is roughly an order of magnitude larger than that of ITO.[10] The figure of merit for CdO (0.133° dB^{-1} T^{-1}) is, however, still substantially smaller than ferromagnetic dielectric materials such as Ce:YIG (943° dB^{-1})[17] and Bi:YIG (769° dB^{-1})[18] at $\lambda = 1.55$ μm. Negative values of F beyond λ_{ENZ} result from the negative Verdet constant in this region (i.e., opposite Faraday rotation).

The rotational figure of merit shown in Figure 3 is not particularly meaningful beyond λ_{ENZ} because the optical response of CdO becomes metallic and light is strongly attenuated (i.e., bulk modes are no longer propagative). Since the MO figure of merit concept implicitly relates to a propagating mode, a better figure of merit in this regime is the nonreciprocal phase shift acquired by the surface plasmon polariton (SPP) mode within one propagation length, L_{spp}:

$$F_{spp} \equiv \mathrm{Re}\left[\Delta k_{spp}\right] L_{spp} = \frac{\mathrm{Re}\left[\Delta k_{spp}\right]}{2 \cdot \mathrm{Im}\left[k_{spp}\right]} \tag{8}$$

where $k_{spp} = (\omega/c)\sqrt{\varepsilon_d \varepsilon_m/(\varepsilon_d + \varepsilon_m)}$ is the (complex) in-plane SPP wavevector[35] that depends on the metal and dielectric permittivity functions, ε_m and ε_d, on either side of the interface. As discussed in ref. [36], an in-plane magnetic field oriented transverse to the SPP propagation direction leads to a frequency shift, $\Delta\omega = \pm\omega_c \sqrt{\varepsilon_m}/(\varepsilon_d^2 + \varepsilon_m^2)$, between forward and backward-going SPPs, which in turn yields a nonreciprocal difference, Δk_{spp}, between the forward and backward propagation constants as illustrated in **Figure** 4a. Note that the SPP mode exists beyond the light line and therefore would require some method of momentum matching such as, for example Kretschmann coupling with a prism, to experimentally measure Δk_{spp}. Figure 4b,c respectively show Δk_{spp} and L_{spp} for the each of the CdO samples interfaced with air ($\varepsilon_d = 1$). The non-reciprocal shift in propagation constant peaks sharply just beyond λ_{ENZ} (at the surface plasmon frequency asymptote, $\omega_p/\sqrt{1+\varepsilon_\infty}$ in Figure 4a), whereas the propagation length increases monotonically with wavelength due to the decreased loss at lower frequency. The combination of these factors leads to a relatively broad peak in F_{spp} that is more than ten times higher than that for ITO (Figure 4d). The outstanding magneto-plasmonic figure of merit for CdO, combined with the ability to precisely control its doping concentration in, for example, multilayer stacks[37] deposited on Si, presents a unique opportunity to develop new MIR integrated magneto-plasmonic devices.[9,24,38]

4. Discussion

Although it seems plausible that doping with strongly paramagnetic Gd might provide an additional contribution to the MO response of, for example, the highest doped Gd sample (S2), where Gd accounts for ≈2% of the lattice sites, the fact that replacing Gd with an equivalent concentration of non-magnetic In (S7) does not appreciably change the Verdet constant argues against this. Taken together with the accuracy of the Drude model in Figure 1c, it seems clear that the MO response of Gd:CdO originates solely from its free electrons.

In this context, it is worth pointing out that the absolute Faraday rotation of CdO does not saturate at high magnetic fields (**Figure** 5a). This is in contrast to ferromagnetic MO materials such as Ce:YIG, which typically saturate at ≈0.1 T.[17,18] Thus, although CdO is not competitive with Ce:YIG in the NIR, its high field capability, combined with the natural falloff in Ce:YIG rotation at longer wavelength, do make it a compelling solution for the MIR. Figure 5b highlights the MIR gap that CdO could fill between YIG-based materials in the NIR and doped InSb in the long wave IR (the 0.17 eV bandgap of InSb limits its operation to $\lambda > 7.2$ μm).

Given that the MIR potential of CdO is based on measured data that only extends to 1.7 μm, it is important to address the uncertainty associated with the Drude model extrapolation. This is captured by the shaded confidence bands in Figure 5b, which show the range of values that fall within the collective Drude parameter error bars for each sample. We did try to extend our Faraday rotation measurements to 2.6 μm using a home-built InGaAs balanced photodiode in order to verify the peak of the highest doped CdO samples (S1 and S2 in Figure 2a). However, due to the substantial decrease in detectivity of the low bandgap component photodiodes (due to their correspondingly higher dark current) and the limited optical power available from our monochromated supercontinuum source, we were unable to resolve the Faraday rotation signal in this case. Redesigning the balanced photodiode to incorporate liquid nitrogen cooling, or using a laser system with more power in the MIR would provide a path to overcome this difficulty in future work.

5. Conclusion

In summary, we have investigated Faraday rotation in doped CdO and found that its Verdet constant peaks close to the ENZ frequency, with values > $3{\bullet}10^5$ deg T^{-1} m^{-1} achievable across the MIR spectrum by varying the doping concentration. These results are in good agreement with the Drude model, which confirms that the MO response derives from free carriers and predicts that further improvement is possible for CdO films with

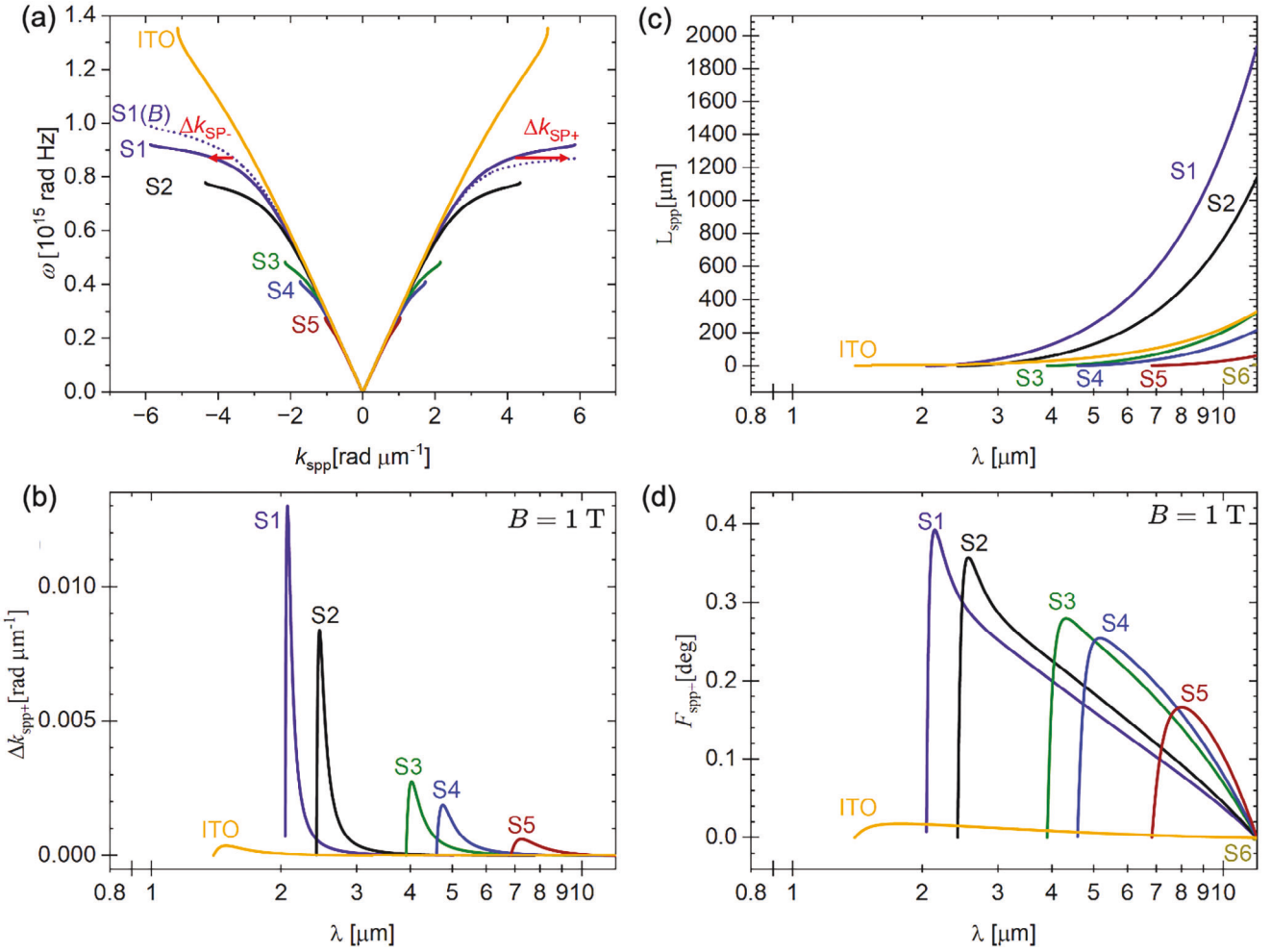

Figure 4. a) Dispersion relation for forward- and backward-propagating surface plasmon polaritons at a CdO/air interface in the presence and absence of a magnetic field. The nonreciprocal phase shift in (b), multiplied by the SPP propagation length in (c), yields the magneto-plasmonic figure of merit in (d). All simulations are carried out at B = 1 T except for the dashed S1 curve in (a), where B = 200 T is used to more clearly illustrate the difference in forward- and backward-going propagation constants that results from the applied magnetic field.

higher optical mobilities, such as those doped with yttrium or fluorine.[39,40] The combination of a tunable Verdet constant, low optical loss compared to other plasmonic materials, and the ability to deposit CdO on Si with no loss in performance makes this material a promising platform for integrated magneto-optic and magneto-plasmonic devices that operate across the MIR spectrum.

6. Experimental Section

Fabrication: Doped CdO thin films are grown through a reactive co-sputtering process in a mixed argon (20 sccm) and oxygen (14.4 sccm) environment at 14 mTorr total pressure. CdO is deposited from a 2-in diameter 99.9999% pure Cd target by reactive high-power impulse magnetron sputtering (HiPIMS) (Starfire Industries Impulse Pulsed Power Module and Advanced Energy MDX 1.5 K DC power supply). The HiPIMS drive conditions are 800-Hz frequency and 80-μs pulse time, producing a 1250-μs period and 6.4% duty cycle. Dopants are incorporated from 2-in diameter 99.99% Gd and In targets using radio frequency (RF) magnetron sputtering (RF VIII RFMN-100-XIII power supply), where RF power is controlled between 0 and 40 W, yielding estimated dopant concentrations between 0.01–2.8% (sample S6-S1). Magnetrons are oriented in a sputter-down geometry at a ≈45° incidence angle, with the substrates (c-Al_2O_3, (100) Si, BK7 glass) adhered by silver paint (Ted Pella) and heated to 200 °C prior to and during deposition using a radiative sample heater. Films are grown on single-side (SSP) and double-side polished (DSP) substrates simultaneously to ensure identical doping conditions between SSP samples used in ellipsometry measurements and DSP samples used in Faraday rotation measurements. To slightly improve μ_{opt} and crystal quality, the samples are annealed after deposition at 635 °C for 30 min in pure oxygen; however, this step is not essential. These processing conditions have been demonstrated in previous reports to yield optimal CdO film quality.[39–41]

Processing parameters (i.e., deposition time and RF power for varying doping levels) are determined by first depositing a test sample (≈100 nm) and characterizing film thickness and transport properties. Film thickness is measured using X-ray reflectivity (XRR) ω–2θ scans via a PANalytical Empyrean X-ray diffractometer in a parallel beam geometry with a double-bounce monochromator and a parallel-plate collimator. The deposition rate from this measurement is extrapolated to determine the deposition time for the thicker samples used in Faraday rotation experiments. Transport properties for the thinner test samples are quantified in the van der

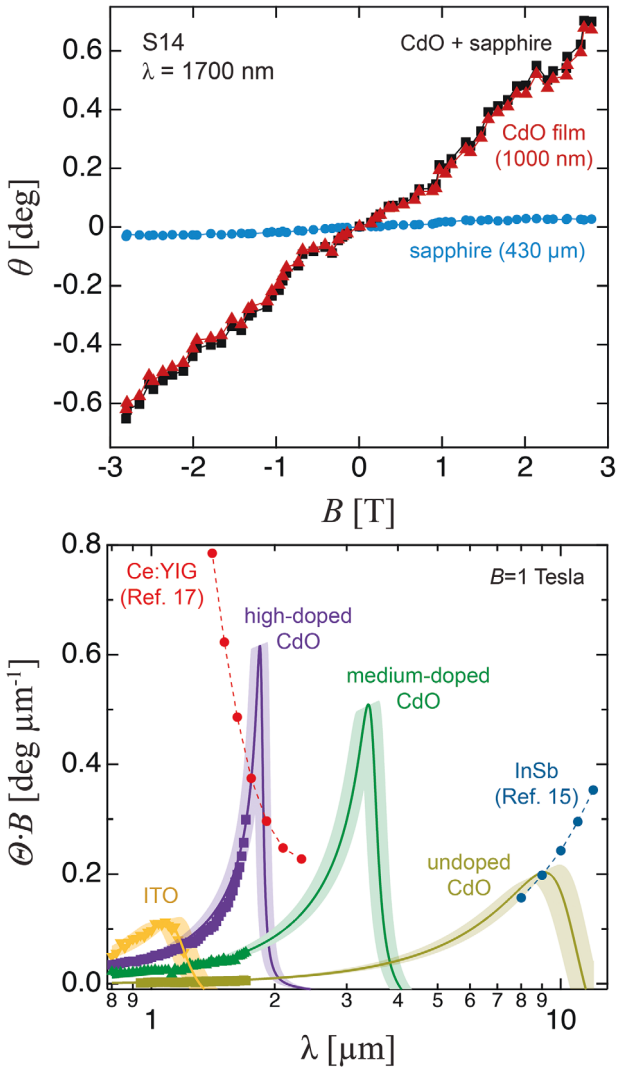

Figure 5. a) Faraday rotation measurement of Sample S14 up to B = 3 T at a wavelength of 1700 nm. The rotation of the CdO film itself (red symbols) equals the difference of the film+substrate measurement (black symbols) and the bare substrate measurement (blue symbols). (b) Specific Faraday rotation of Ce:YIG[17] and InSb[15] compared to CdO at B = 1 T, highlighting the MIR "hole" in MO response that doped CdO can fill. The shaded confidence bands superimposed on the CdO curves capture the range of values that fall within the Drude fit parameter uncertainties associated with each sample.

Pauw configuration using an Ecopia HMS-3000 Hall Effect measurement system with a 0.545 T magnet.

Because XRR is not capable of measuring thickness for films greater than a few hundred nanometers, 5% HCl in water is used to etch a clean line in the film to measure over the step edge and determine the film thickness using mechanical profilometry and atomic force microscopy (AFM). The measured thickness values are consistent with those expected from the deposition rates. AFM data is collected using an Asylum Research MFP-3D AFM in tapping mode. Mechanical profilometry was conducted using a KLA-Tencor P16+.

The crystal quality of films is characterized by X-ray diffraction (XRD) θ–2θ patterns in the same geometry used for XRR. Although CdO on c-plane sapphire and (100) Si does not grow epitaxially (Supplementary Material Figure S10, Supporting Information) as in the case of an r-plane sapphire substrate,[41] both films exhibit comparably low surface roughness as seen in cross-sectional scanning electron microscopy (Figure S11a–c, Supporting Information) and AFM surface mapping (≈26–56 nm RMS roughness in Figure S11d–f, Supporting Information).

Drude model fitting of IR variable-angle ellipsometry measurements (IR-VASE, JA Woollam) on each CdO film give the real ε' and imaginary ε'' components of the permittivity, as well as the parameters N, ε_∞, m^*, and μ_{opt} that are needed to model Faraday rotation using Equation (5).[27] In general, the parameters extracted from ellipsometry accurately describe the Faraday rotation data and need only be varied by a small amount (<5%) to achieve the best-fit lines shown in Figures 1, 2, and 5b. Faraday rotation spectroscopy thus offers a useful complementary method of extracting Drude material parameters for TCO films when measured over a sufficiently large bandwidth near their ENZ wavelength. Although μ_{opt} can vary slightly depending on the growth conditions and dopant used, this parameter was the same within the uncertainty of the fits and was therefore fixed at a nominal value of 200 $cm^2\ V^{-1}\ s^{-1}$ for all of the calculations in Figures 1–5 for the sake of transparency.

MO Polarimetry: Faraday rotation spectroscopy is carried out using a benchtop MO polarimeter based on the design published by Gangopadhyay et al.[42] which is illustrated in Supplementary Figure S14 (Supporting Information). A supercontinuum laser (Fianium WhiteLase SC 480) is passed through a 1/8 m monochromator and motorized filter wheel (equipped with longpass filters to absorb the grating double/triple) to produce collimated monochromatic light with a full-width half-maximum bandwidth of ≈8 nm and a beam cross-sectional area of ≈1 cm^2. The beam is subsequently polarized using a calcite Glan-Thompson linear polarizer and sent axially through a pair of 15 cm-long, 560-turn, 6 cm-diameter air-cooled solenoids that produce a uniform magnetic field. The sample (e.g., a CdO film on a substrate or the bare substrate for reference) sits in the beam path between the solenoids. After passing through the sample, the light is reflected off an external silver mirror and sent back through the sample, doubling the Faraday rotation to improve signal-to-noise. A calcite Wollaston prism oriented at 45° to the original linear polarization then splits the beam into vertical (I_V) and horizontal (I_H) polarization components that are focused onto the inputs of a balanced photodiode (Thorlabs PDB210C, 800–1700 nm). A gradient neutral density (ND) filter is mounted on a translation stage in front of one of the photodiode inputs and is adjusted at each wavelength to balance the I_V and I_H photodiode signals for maximum signal-to-noise in the measurement.

The monitor output of each photodiode provides a DC voltage that is proportional to the incident optical power on each, while the RF output amplifies (with a gain of A = 50) the difference signal between the two photodiodes for read out by a lock-in amplifier. The sinusoidal signal of a function generator is boosted with an AC power amplifier to drive the solenoid, with a 1 μF, 2200 V capacitor connected in series to yield an RLC resonance that matches the 1275 Hz drive frequency to maximize power transfer. This arrangement yields an AC magnetic field up to 14 mT: the magnetic field strength is calibrated before each measurement by placing a gaussmeter at the location of the sample.

A typical measurement begins by placing the sample in the beam path at the starting wavelength of interest with no applied magnetic field. Once the photodiodes are balanced using the ND filter, the magnetic field is swept from 0.4–13.6 mT in 0.4 mT steps while the difference between the photodiodes and the total DC signal of each is recorded. This process is repeated across the entire spectrum in λ = 20 nm steps. Both the film on the substrate and the bare substrate itself are measured. The instruments are controlled using Python and the PyVISA package to automate the process.

The Faraday rotation angle per pass through a given sample, θ, is calculated from the measured optical signal via $\theta(\text{degrees}) = (180/\pi)\sqrt{x^2+y^2}/(2AN_{pass}[I^{DC,H}+I^{DC,V}])$, where x and y are the in and out-of-phase components measured by the lock-in amplifier (in Volts), A is the differential gain (labeled RF output) of the detector, and $I^{DC,H}$ and $I^{DC,V}$ are the DC voltage signals measured by each of the photodiodes. The number of passes, N_{pass}, is equal to 2 for this setup, and the other factor of 2 results from the Mueller matrix treatment of time-varying signal lineshape.[42] The rotation angle due only to the film is determined

by the difference between that measured from the film+substrate sample and the bare substrate reference, $\theta_{film} = \theta_{film+substrate} - \theta_{substrate}$. When measuring thin films, the Faraday rotation of air is naturally included in the reference measurement and thus does not need to be measured independently. When measuring the Verdet constant of bare substrates, air should be included, but is a small (<10%) correction in our case.[43]

When the Faraday rotation angle is linear with magnetic field, as is the case for all of the data measured in this work, the Verdet constant (Θ) is calculated for the film or substrate via $\Theta = \theta/(BL)$, where L is the film or substrate thickness. The slope of θ versus B is used to minimize uncertainty in determining Θ as shown in Figures S2b and S3 (Supporting Information).

It is worth noting that birefringent substrates can be problematic in certain instances, and thus all sapphire-based measurements are carried out at normal incidence on c-plane substrates. As described by Kim et al.,[44] another issue that can occur when measuring thin films using an AC MO polarimeter is when the Verdet constant of the film and substrate are opposite in sign, as is the case for CdO and Si. Because only the magnitude of the signal is measured, it can be difficult to tell if the total rotation direction has changed, giving two possible solutions for the Verdet constant. For the measurements on Si in this work, it is clear from agreement with the Drude model prediction and data from CdO on other substrates that the net rotation direction remains constant over the measured spectral range and film thicknesses employed. The Verdet constant of doped CdO was found to be independent of laser power; no significant fraction of free carriers are optically generated under the conditions of these experiments, although it may be possible that other plasmonic materials with substantially lower carrier concentrations have a power-dependent MO response from such an effect.[32]

Supporting Information

Supporting Information is available from the Wiley Online Library or from the author.

Acknowledgements

J.R.S. and N.C.G. were supported by the NSF under Grant Nos. DMR-2011839 and DMR-1654077. A.J.C., M.J.T., and J.P.M. were supported by the Office of Naval Research Grant No. N00014-22-12035 and the Army Research Office Grant No. W911NF-21-1-0119.

Conflict of Interest

The authors declare no conflict of interest.

Data Availability Statement

The data that support the findings of this study are available from the corresponding author upon reasonable request.

Keywords

ENZ, Faraday rotation, isolator, transparent conducting oxide, Verdet constant

Received: March 23, 2024
Revised: July 17, 2024
Published online: August 5, 2024

[1] W. Jaffray, S. Saha, V. M. Shalaev, A. Boltasseva, M. Ferrera, *Adv. Opt. Photonics* **2022**, *14*, 148.
[2] G. V. Naik, V. M. Shalaev, A. Boltasseva, *Adv. Mater.* **2013**, *25*, 3264.
[3] R. Amin, R. Maiti, Y. Gui, C. Suer, M. Miscuglio, E. Heidari, J. B. Khurgin, R. T. Chen, H. Dalir, V. J. Sorger, *Sci. Rep.* **2021**, *11*, 1287.
[4] V. E. Babicheva, A. Boltasseva, A. V. Lavrinenko, *Nanophotonics* **2015**, *4*, 165.
[5] M. Z. Alam, I. De Leon, R. W. Boyd, *Science* **2016**, *352*, 795.
[6] O. Reshef, I. De Leon, M. Z. Alam, R. W. Boyd, *Nat. Rev. Mater.* **2019**, *4*, 535.
[7] N. Kinsey, J. Khurgin, *Opt. Mater. Express* **2019**, *9*, 2793.
[8] S. Campione, M. G. Wood, D. K. Serkland, S. Parameswaran, J. Ihlefeld, T. S. Luk, J. R. Wendt, K. M. Geib, G. A. Keeler, *IEEE Photonics J.* **2017**, *9*, 1.
[9] A. Gabbani, C. Sangregorio, B. Tandon, A. Nag, M. Gurioli, F. Pineider, *Nano Lett.* **2022**, *22*, 9036.
[10] K. Ikeda, T. Liu, Y. Ota, N. Kobayashi, S. Iwamoto, *Adv. Opt. Mater.* **2024**, *12*, 2301320.
[11] H. Feil, C. Haas, *Phys. Rev. Lett.* **1987**, *58*, 65.
[12] E. Ferguson, O. M. Stafsudd, R. F. Wallis, *Physica B+ C* **1977**, *89*, 91.
[13] V. I. Safarov, V. A. Kosobukin, C. Hermann, G. Lampel, J. Peretti, C. Marlière, *Phys. Rev. Lett.* **1994**, *73*, 3584.
[14] S. V. Tomilin, A. V. Karavaynikov, S. D. Lyashko, E. T. Milyukova, O. A. Tomilina, A. S. Yanovsky, V. I. Belotelov, V. N. Berzhansky, *Opt. Mater. Express* **2022**, *12*, 1522.
[15] N. Peard, D. Callahan, J. C. Perkinson, Q. Du, N. S. Patel, T. Fakhrul, J. LeBlanc, C. A. Ross, J. Hu, C. Y. Wang, *J. Appl. Phys.* **2021**, *129*, 203104.
[16] K. J. Shayegan, B. Zhao, Y. Kim, S. Fan, H. A. Atwater, *Sci. Adv.* **2022**, *8*, eabm4308.
[17] M. C. Onbasli, L. Beran, M. Zahradnık, M. Kučera, R. Antoš, J. Mistrık, G. F. Dionne, M. Veis, C. A. Ross, *Sci. Re* **2016**, *6*, 23640.
[18] T. Fakhrul, S. Tazlaru, L. Beran, Y. Zhang, M. Veis, C. A. Ross, *Adv. Opt. Mater.* **2019**, *7*, 1900056.
[19] T. Haider, *Int. J. Electromagn. Appl.* **2017**, *7*, 17.
[20] K. Srinivasan, B. J. H. Stadler, *Opt. Mater. Express* **2022**, *12*, 697.
[21] T. Mizumoto, R. Baets, J. E. Bowers, *MRS Bull.* **2018**, *43*, 419.
[22] M. Al-Mahmoud, H. Hristova, V. Coda, A. A. Rangelov, N. V. Vitanov, G. Montemezzani, *OSA Continuum* **2021**, *4*, 2695.
[23] T. Arikawa, X. Wang, A. A. Belyanin, J. Kono, *Opt. Express* **2012**, *20*, 19484.
[24] J. Qin, S. Xia, W. Yang, H. Wang, W. Yan, Y. Yang, Z. Wei, W. Liu, Y. Luo, L. Deng, L. Bi, *Nanophotonics* **2022**, *2*, 2639.
[25] J.-M. Fedeli, S. Nicoletti, *Proc. IEEE Inst. Electr Electron. Eng.* **2018**, *106*, 2302.
[26] Y. Zou, S. Chakravarty, C.-J. Chung, X. Xu, R. T. Chen, *Photonics Res.* **2018**, *6*, 254.
[27] J. R. Nolen, E. L. Runnerstrom, K. Kelley, T. S. Luk, T. G. Folland, A. Cleri, J.-P. Maria, J. D. Caldwell, *Phys. Rev. Mater.* **2020**, *4*, 025202.
[28] O. Morikawa, A. Quema, S. Nashima, H. Sumikura, T. Nagashima, M. Hangyo, *J. Appl. Phys.* **2006**, *100*, 033105.
[29] C. Liu, Y. Foo, M. Kamruzzaman, C. Y. Ho, J. A. Zapien, W. Zhu, Y. J. Li, W. Walukiewicz, K. M. Yu, *Phys. Rev. Appl.* **2016**, *6*, 064018.
[30] H. Fujiwara, M. Kondo, *Phys. Rev. B* **2005**, *71*, 075109.
[31] A. R. Taussig, G. F. Dionne, C. A. Ross, *Phys. Rev. B* **2008**, *77*, 012407.
[32] A. K. Zvezdin, V. A. Kotov, *Modern Magnetooptics and Magnetooptical Materials*, CRC Press, New York **1997**.
[33] E. Sachet, C. T. Shelton, J. S. Harris, B. E. Gaddy, D. L. Irving, S. Curtarolo, B. F. Donovan, P. E. Hopkins, P. A. Sharma, A. L. Sharma, J. Ihlefeld, S. Franzen, J.-P. Maria, *Nat. Mater.* **2015**, *14*, 414.
[34] D. Vojna, O. Slezák, R. Yasuhara, H. Furuse, A. Lucianetti, T. Mocek, *Materials* **2020**, *13*, 5324.
[35] H. Raether, *Surface Plasmons on Smooth and Rough Surfaces and on Gratings*, Springer, New York, **1988**.
[36] A. J. Cleri, J. R. Nolen, K. G. Wirth, M. He, E. L. Runnerstrom, K. Kelley, J. Nordlander, T. Taubner, T. G. Folland, J.-P. Maria, *Adv. Optic. Mater.* **2023**, *11*, 2202137.

[37] E. L. Runnerstrom, K. Kelley, T. G. Folland, J. R. Nolen, N. Engheta, J. D. Caldwell, J.-P. Maria, *Nano Lett.* **2018**, *19*, 948.
[38] K. Kelley, E. L. Runnerstrom, E. Sachet, C. T. Shelton, E. D. Grimley, A. Klump, J. M. LeBeau, Z. Sitar, J. Y. Suen, W. J. Padilla, J.-P. Maria, *ACS Photonics* **2019**, *6*, 1139.
[39] K. Kelley, E. Sachet, C. T. Shelton, J.-P. Maria, *APL Mater.* **2017**, *5*, 076105.
[40] E. L. Runnerstrom, K. Kelley, E. Sachet, C. T. Shelton, J.-P. Maria, *ACS Photonics* **2017**, *4*, 1885.
[41] K. Y. Bliokh, F. J. Rodríguez-Fortuño, A. Y. Bekshaev, Y. S. Kivshar, F. Nori, *Opt. Lett.* **2018**, *43*, 963.
[42] Gangopadhyay, R. Voorakaranam, A. Lopez-Santiago, S. Foerier, J. Thomas, R. A. Norwood, A. Persoons, N. Peyghambarian, *J. Phys. Chem. C* **2008**, *112*, 8032.
[43] G. Phelps, J. Abney, M. Broering, W. Korsch, *Rev. Sci. Instrum.* **2015**, *86*, 073107.
[44] Y. Kim, D. J. Bang, Y. Kim, K. H. Kim, *AIP Adv.* **2020**, *10*, 025306.